Miyanaga and Yamanaka
Earth, Planets and Space (2023) 75:135
https://doi.org/10.1186/s40623-023-01884-7

Earth, Planets and Space

FULL PAPER

Open Access

Effects of surface topography and subsurface structural irregularities of river embankments on Rayleigh wave propagation

Shuntaro Miyanaga[1*] and Hiroaki Yamanaka[2]

Abstract

A numerical investigation of surface wave propagation in the surface wave exploration of river embankments is implemented using 3D shallow soil models with different subsurface shapes and S-wave velocities. The focus is on the effects of surface and subsurface irregularities on the propagation and dispersion characteristics of Rayleigh waves generated by a surface source and observed at points along the crest of the embankment. Rayleigh wave dispersion curves observed along the embankment crest are found to be contaminated by reflected waves, with the amount of contamination affected more by the position of the velocity boundary at the bottom edge of the embankment than the surface topography. When the velocity boundary is close to the ground surface, especially at the toe of the slope, the effect of reflected waves is sufficiently large to generate biases in the phase velocity estimates.

Keywords Surface wave exploration, S-wave velocity, River embankment, Rayleigh wave, Dispersion curve

*Correspondence:
Shuntaro Miyanaga
mynsnt00@pub.taisei.co.jp
Full list of author information is available at the end of the article

Graphical Abstract

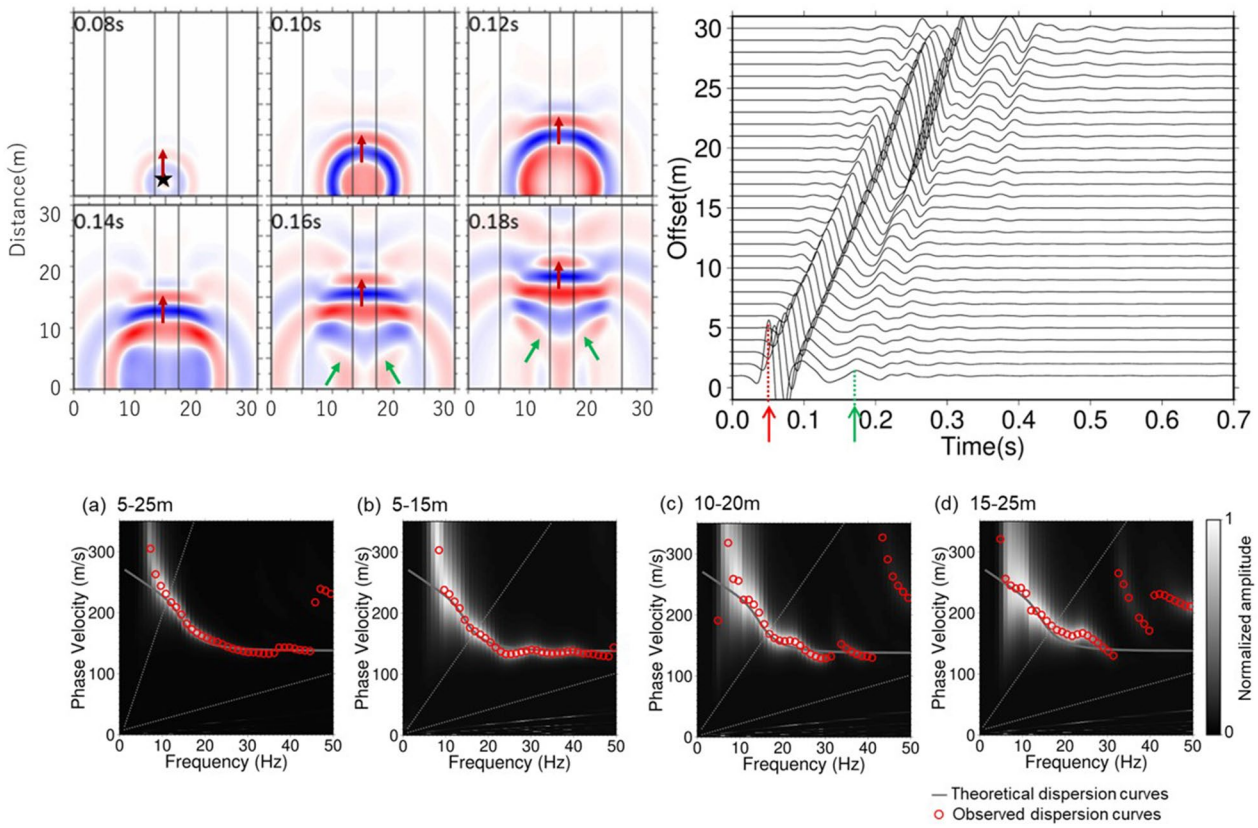

Main text

Introduction

Surface wave exploration is a method used in various geotechnical and geophysical fields for estimating a subsurface S-wave velocity profile in shallow soil layers using the dispersive property of surface waves. Rayleigh waves are generally used because they are easily generated by vertical impacts (e.g., Socco et al. 2010). More than two-thirds of the seismic energy propagates as Rayleigh waves in the case of a vertical impulsive force on the surface, such as with a sledge hammer or a dropped weight (e.g., Richart et al. 1970). Since a phase velocity dispersion of Rayleigh waves is frequency-dependent and also related with a S-wave velocity distribution beneath an observation point (e.g., Okada 2003), a 1D subsurface S-wave velocity profile in the depth direction can usually be estimated from the dispersive features of the phase velocity.

Nazarian et al. (1983) introduced a method of spectral analysis of surface waves (SASW) to estimate a 1D S-wave velocity profile to a depth of 100 m from Rayleigh wave phase velocities recorded at two receivers. This method has been used in many geotechnical engineering fields (e.g. Stokoe et al. 1994). Park et al. (1999) proposed the multichannel analysis of surface waves (MASW) to determine phase velocities directly from surface wave data at many points. This method has widely been used in soil surveys of, for example, river embankments, landfill and residential land. In MASW, Rayleigh wave phase velocity dispersion curves are estimated with several methods: the F-K transform (e.g. Yilmaz 1987), the tau-p transform (McMechan and Yedlin 1981), phase shift (Park et al. 1998) and the slant stacking algorithm (Xia et al. 2007). Then, a 1D S-wave profile is obtained from an inversion of the dispersion curve (e.g., Xia et al. 1999). A 2D S-wave velocity structure may be also constructed by synthesizing 1D profiles (Miller et al. 1999; Xia et al. 2004; Hayashi and Suzuki 2004; Luo et al. 2009).

In data analysis in the surface wave method, we usually assume a horizontally layered model with a flat ground surface (Xia et al. 1999). Namely, the surface wave theory

for a horizontally layered model is used for analysis even if the soil layers actually have surface and subsurface irregularities. An irregularity near an observation point causes wave-scattering that may contaminate the Rayleigh wave dispersion curve that would be expected in a horizontally layered model. Several studies have investigated the applicability of the surface wave analysis to soil layers with surface irregularities or subsurface structural irregularities. Hayashi and Inazaki (2007) performed a numerical experiment with 3D numerical models as well as a field test to investigate the effects of the slope of a river embankment on surface wave propagation. This work confirmed that the effects of the slope on the surface wave dispersion curves were minor. Kim et al. (2010) performed numerical experiments of surface wave propagation at the crest and on the inclined face of an existing rock-fill dam, and verified the applicability of the surface wave method in this case. In order to improve the dispersion curve estimation in the analysis, Hayashi and Suzuki (2004) proposed using common midpoint cross-correlation analysis (CMPCC) in which mulch-channel and multi-shot surface data are used in a cross-correlation. This method can improve the accuracy and resolution of Rayleigh wave phase velocities in a model with a lateral variation in S-wave velocity along an observation line. In fact, most previous studies have focused on examining the applicability of the surface wave method at sites with surface or subsurface velocity variations in the direction of the observation line. However, their effects in the direction perpendicular to the observation line have not been sufficiently investigated.

In this study, we conduct numerical experiments to investigate the effects of surface topography and subsurface velocity irregularities in river embankment models on the propagation of Rayleigh waves generated by a surface source. In particular, we discuss the effect on the surface wave dispersion of reflected waves resulting from 3D irregularity that is present outside the observation line. We use a 3D finite difference method (FDM) to calculate synthetic data in the experiments. The characteristics of the wave propagation and the Rayleigh wave dispersion features are discussed on the basis of the synthetic data to verify the assumption of a horizontally layered structure as often used in the surface wave exploration.

Method

Models

We created 3D shallow soil models with shapes similar to a river embankment. Although embankments may have inside layers with lower S-wave velocity than the surface layer (Hayashi and Inazaki 2007), we consider only two-layer models in which the S-wave velocity of the first layer is smaller than that of the second layer. Figure 1 shows the cross-sections of the two models. The physical parameters are constant along the longitudinal axis of the models. Embankment height and crest width are fixed at 4 m in both models, and the ratio of the height to the horizontal slope length is 1:2. The transverse direction of the embankment models is defined as the X axis, the longitudinal direction is regarded as the Y axis. The vertical direction is the Z axis. In model A, shown in Fig. 1a, the boundary between the first and second layers is horizontal at the central part of the embankment, and terminated at the bottom edges in the left and right sides. On the other hand, in model B, as shown in Fig. 1b, the boundary is not horizontal and the bottom edges are not included. The thickness of the first layer just below the crest of the embankment is 4 m in the two models. In both models, the P-wave and S-wave velocities of the first layer are 260 m/s and 150 m/s, respectively, assuming that P-wave velocity is 1.73 times the S-wave velocity. We, furthermore, assume the density of the first layer is 1600 kg/m^3. Table 1 shows the physical parameters of the models. We do not consider any attenuation in the model.

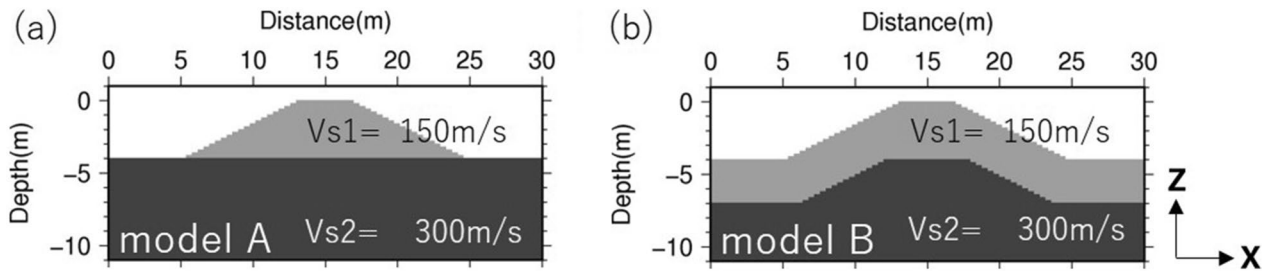

Fig. 1 Cross-sections of embankment models used in numerical experiments. Embankment height and crest width are 4 m. The gradient of the embankment slope is 1:2. The first layer immediately below the embankment crest has the same depth in both models. **a** Model A. The boundary between the first and second layers is horizontal and at the bottom of the embankment. **b** Model B. The boundary is not horizontal and is partially in the subsurface

Finite difference calculation

We employed a 3D staggered grid FDM (Graves 1996) of the second-order accuracy in time and the 8th-order accuracy in space to generate synthetic waves. The volume of the model is 75 m (L)×75 m (W)×37.5 m (D). The finite difference (FD) grid spacing is 0.125 m in all directions and the number of grid points per shortest wavelength is 24. The time step, Δt, was determined for each velocity model using the following formula.

$$\Delta t < 0.669 \frac{h}{v_{\mathrm{pmax}}\sqrt{3}}, \tag{1}$$

where v_{pmax} is the maximum P-wave velocity of the model and h is the grid spacing. To avoid artificial reflections from the edges of the numerical models, we defined an absorbing boundary (Clayton and Engquist 1977) and a buffer region (Cerjan et al. 1985) on the four sides and the bottom of each model. A vacuum formulation (Zeng et al. 2012) was employed to satisfy the free-stress condition on the model surface; that is, the P- and S-wave velocity and density on the model surface were set to zero.

In the numerical experiments, we analyzed the synthetic vertical waves in a frequency range of 5–50 Hz. In order to reduce the effects of the numerical dispersion of the synthetic waves in the finite difference (FD) calculation, a sufficient number of the grid points per minimum wavelength is required (e.g., Mittet 2002). Hence, to validate the relationship between the accuracy of the FD approximation and the grid spacing, we conducted a numerical test as detailed in the Appendix. The synthetic waves were generated on the surface of a homogeneous model with several choices of the FD approximation in terms of the order of the spatial finite difference and the grid intervals. This confirmed that the synthetic wave amplitudes remain stable if the FD accuracy of the spatial partial derivatives is more than 4th-order and the number of the grid points per the minimum wavelength exceeds 15. In consideration of reasonable computing time, the 8th-order spatial derivative accuracy was selected with a grid spacing of 0.125 m. As already noted, the number of the grid points per the shortest wavelength (at 50 Hz) was 24.

Source and observation points

The source was placed on the embankment crest as shown in Fig. 2a. A Ricker wavelet with a central frequency of 20 Hz was applied as the source-time function for the vertical source on the surface in order to simulate an impulsive impact such as with a hammer. The Ricker wavelet is defined by

$$w(t) = \left[1 - 2\pi^2 f^2 (t - t_0)^2\right] \exp(-\pi^2 f^2 (t - t_0)^2, \tag{2}$$

where f is the peak frequency, t is the time variable, and t_0 is the time delay. Synthetic waveforms were calculated for a duration of 0.7 s. One set of observation points was placed linearly along the center of the embankment crest at a spacing of 1 m, as marked by (1) in Fig. 2a; the vertical component of the synthetic ground velocity was calculated at each point. We also placed two circular arrays on the crest, as marked by (2) and (3) in Fig. 2a, at distances of 12.5 m and 22.5 m from the source, respectively. The observation points in these two arrays are indicated

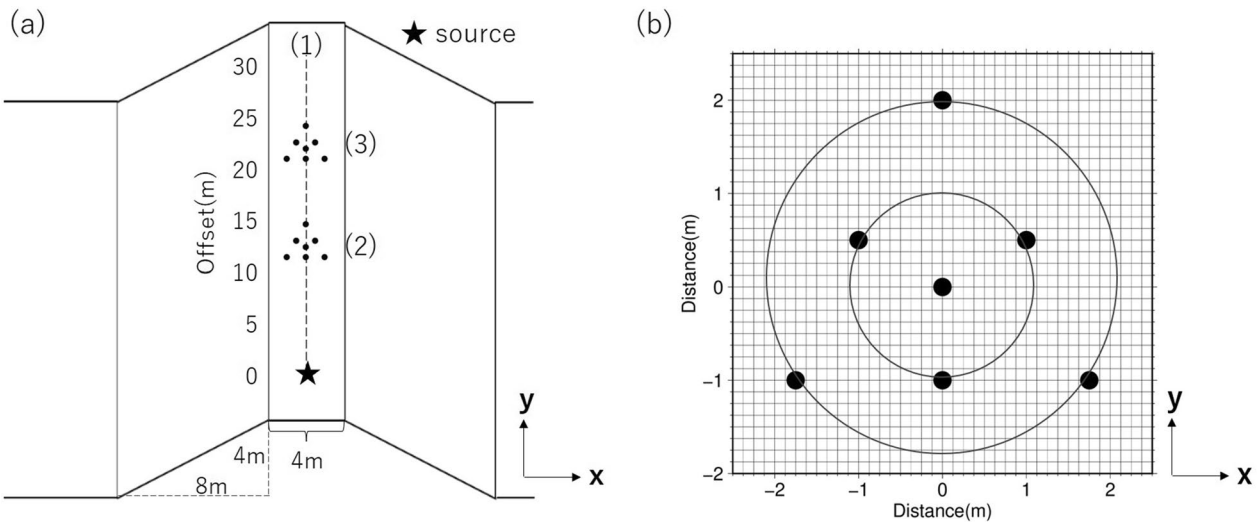

Fig. 2 Location of surface source (star) and observation points (solid circles). **a** Overview of source location, linear array (1) and circular arrays (2), (3). **b** Configuration of circular arrays

in Fig. 2b. The purpose of these two arrays is to understand the propagation direction of scattered and reflected waves that may be generated by the surface and subsurface irregularities.

Results of numerical tests with model A

Synthetic waveforms

Firstly, we explain the results of the numerical experiments using model A. Figure 3a shows snapshots of the synthetic velocities on the ground surface. Red arrows in the figure represent the arrival of the Rayleigh wave that propagates along the surface from the source. We describe these as "direct Rayleigh waves". Green arrows show that the direct Rayleigh wave is scattered or reflected at the bottom edges of the embankment and propagates back to the crest again. Thus, in this paper, we call these "reflected Rayleigh waves". Figure 3b shows snapshots of the synthetic velocities of the embankment cross-section including the source point. Green arrows represent waves that are reflected at the bottom edges of the embankment and propagate back to the crest.

Figure 4 shows the vertical components of the synthetic velocities as recorded by the linear array. The red arrow marks the initial rise point of the direct Rayleigh wave propagating along the embankment crest from the source, while the later phase indicated by the green arrow represents the arrival of the reflected Rayleigh waves. The direct and reflected Rayleigh waves can be easily defined by their arrival times at the points near the source. However, as the distance from the source increases, the phases of these waves overlap because of similar their arrival times.

Rayleigh wave dispersion curves

Dispersion curves of the phase velocities were estimated from the synthetic vertical motions for model A using

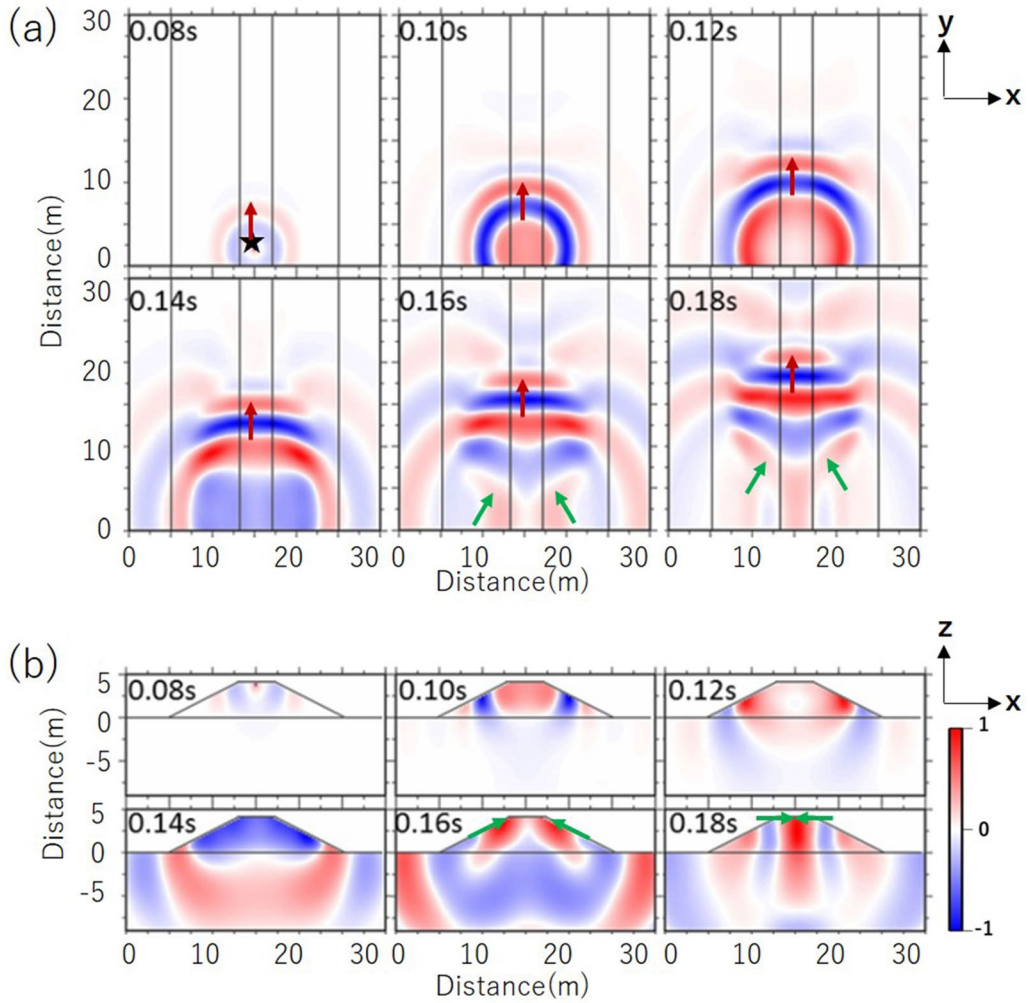

Fig. 3 Snapshots of synthetic vertical velocities (**a**) on the surface and (**b**) in cross-section including the source point of model A. Colors represent the amplitude of the vertical component. Red and green arrows indicate the direct wave and reflected Rayleigh waves, respectively

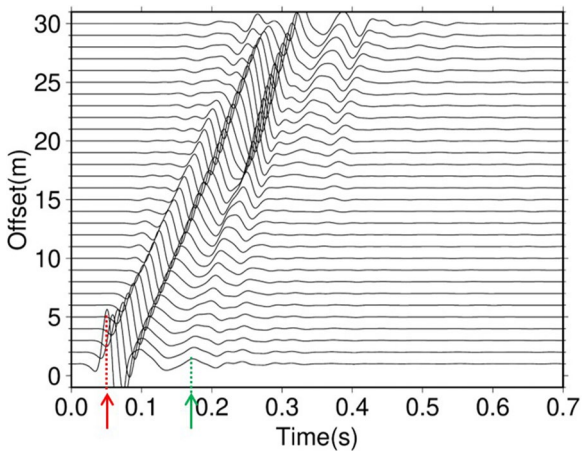

Fig. 4 Synthetic vertical velocities along the linear array on the crest of model A. Red and green arrows indicate the direct wave and reflected Rayleigh waves, respectively

an F-K transformation (e.g. Yilmaz 1987). To investigate the effects of the reflected Rayleigh waves and the source offset distances on the dispersion curves, the synthetic waves at source distance ranges of 20 or 10 m (5–25 m, 5-15 m, 10–20 m, 15–25 m) along the linear array were analyzed. The synthetic waves generated over a duration of 0.7 s were used for this analysis.

Figure 5 shows the dispersion images of the synthetic velocities shown in Fig. 4 in the frequency-velocity domain. The gray shading in the figure represents the normalized power at each frequency and phase velocity, while the open red dots indicate the derived dispersion curve of the phase velocity with the maximum power. The solid line represents the theoretical dispersion curve of the fundamental mode Rayleigh waves for the 1D profile beneath the center of the arrays in model A. The two dotted lines indicate the phase velocity from the capable maximum wavelength of Rayleigh waves which is same as the array length, and the capable minimum one which is twice the array spacing (Foti et al. 2017). We focus only on the frequency band between the two dotted lines which is the capable wavelength. The observed dispersion curve for the waves in the range of 5–25 m (Fig. 5a) fits well with the theoretical dispersion curve at frequencies below 45 Hz. However, the phase velocities are larger than the theoretical values at frequencies higher than 45 Hz. Thus, the effect of the reflected Rayleigh wave may be large at high frequency. The observed dispersion curves in a distance range of 5–15 m fit well with the theoretical ones at any frequencies, as shown in Fig. 5b. Indicating minor effect of reflected Rayleigh waves. However, the differences between the observed and theoretical dispersion curves in Fig. 5c (10–20 m) are large at frequencies more than 40 Hz. In particular, the discrepancy between the two values is more than 80 m/s at frequencies of 40 to 50 Hz. The theoretical wavelength of the fundamental mode Rayleigh waves in this frequency band is about 3 m. This means that the contribution of the reflected Rayleigh waves to the wave field is larger than that of the direct Rayleigh waves when the distance from the source is more than about five times the wavelength of the Rayleigh waves.

A large discrepancy is also seen in the phase velocity at a distance range of 15–25 m (Fig. 5d). The difference is about 30 m/s at frequencies of about 24 Hz, and 30 to 130 m/s at frequencies of 35 to 50 Hz. The wavelength of the Rayleigh wave at a frequency of 24 Hz is about 6 m, and the distance from the source is 2.5 times the wavelength for the Rayleigh wave. When the wavelength of the observed Rayleigh wave is not very short as compared with the distance from the source, the direct Rayleigh wave cannot be contaminated by the reflected Rayleigh waves.

Wave propagation characteristics

F-K power spectra (Capon 1969) were calculated from the synthetic waves recorded in the circular arrays to investigate the propagation direction of the waves. Figure 6 shows the F-K spectra at frequencies of 15.9, 26.8, 36.6 and 47.6 Hz in the two circular arrays marked as (2) and (3) in Fig. 2a. The horizontal and vertical axes represent the wavenumbers in the perpendicular and longitudinal axes of the embankment, respectively. The gray shading in the figure indicates the normalized power of the synthetic velocity at each wavenumber. The F-K spectra from the circular array (2) show only a single peak related to the direct Rayleigh waves propagating in the longitude direction at each frequency, as shown by the red rings in Fig. 6a–d. Similarly, for the circular array (3), only single peaks of the direct Rayleigh waves are seen at frequencies of 15.9 Hz, 26.8 Hz and 36.6 Hz (Fig. 6e–g). On the other hand, three peaks can be identified in the F-K spectrum at a frequency of 47.6 Hz in Fig. 6h. The two peaks marked with green rings in the figure correspond to arrivals of the reflected surface waves from the velocity boundary at the bottom edges of the embankment, which propagate at an angle to the longitudinal axis. The white dotted line of Fig. 6h represents the wavenumber of the fundamental mode Rayleigh wave. These results indicate that the waves observed at points far from the source are more contaminated by the fundamental mode of Rayleigh waves generated at the bottom edges of the embankment, especially at a high frequency.

Dispersion curves at high frequency

Because the significant effect of reflected Rayleigh waves on the dispersion curves was identified in the

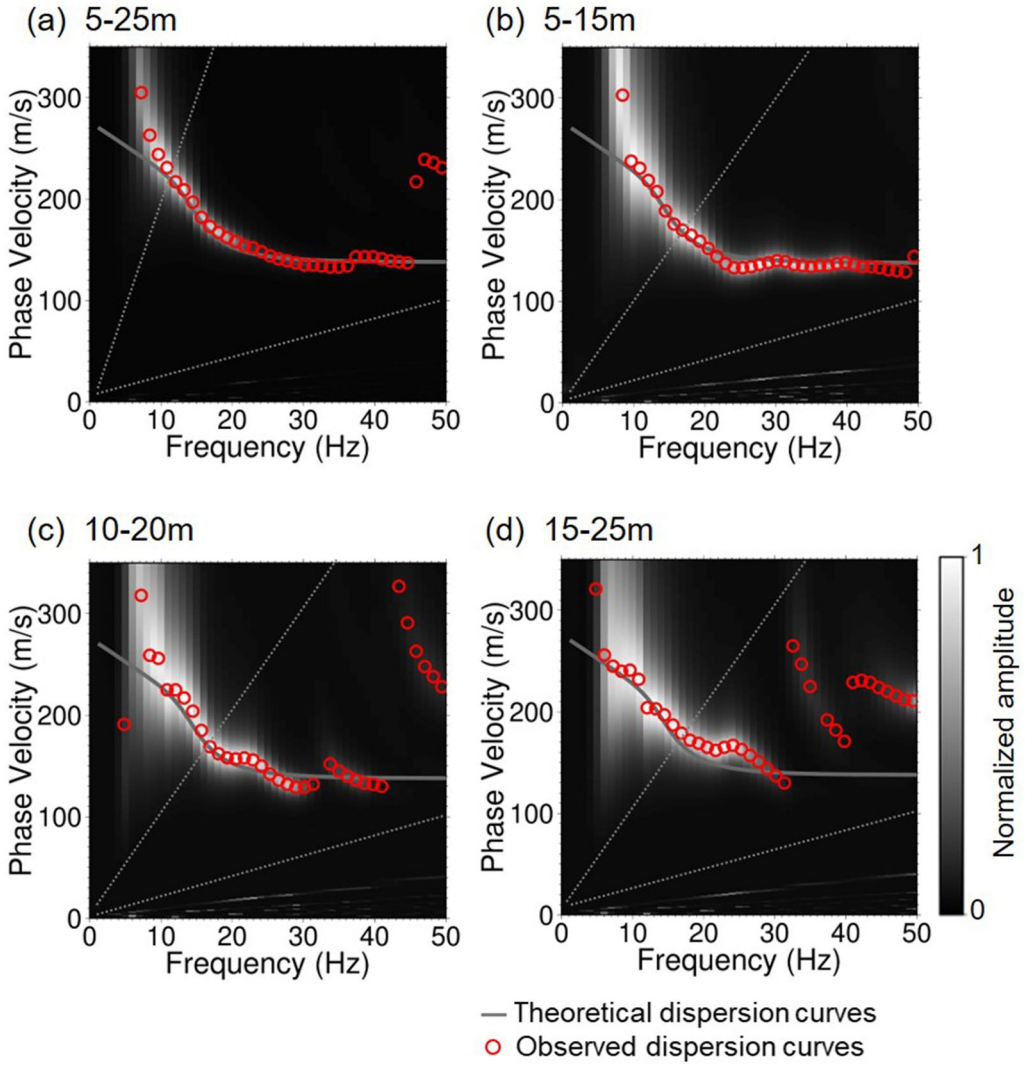

Fig. 5 Rayleigh wave phase velocities from vertical motions in Fig. 4. Phase velocity analysis of synthetic waveforms in 20 or 10 m ranges from the source: **a** 5–25 m, **b** 5–10 m, **c** 10–20 m; and **d** 15–25 m. Gray shading represents normalized power of synthetic velocity at each frequency. Open red dots represent observed phase velocity. Solid lines are the theoretical dispersion curves of the Rayleigh wave fundamental mode for model A. The two dotted lines indicate the maximum and minimum wavelengths resolved by the linear array. The frequency bands of capable wavelength are focused

wave fields at the high frequency (Fig. 5), we calculated dispersion curves for every 5 m ranges along the survey line to focus on the high-frequency components. Figure 7 shows the dispersion curves of the synthetic waves recorded in the ranges of 5–10 m, 8–13 m, 11–16 m, 14–19 m, 17–22 m and 20–25 m from the source. The plotted points and solid line represent the observed and theoretical phase velocities, respectively. The two dotted lines indicate the phase velocity estimated from the capable maximum and minimum wavelengths of Rayleigh wave. The dispersion curves of the phase velocity obtained from the synthetic waves at relatively small distances from the source (in the ranges 5–10 m and 8–13 m) fit well with the theoretical ones at any frequency. In the distance range of 11–16 m, the differences in the phase velocity are more than 100 m/s at frequencies above 45 Hz. At greater distances (in the ranges 14–19 m, 17–22 m and 20–25 m), these differences in the phase velocity are larger at frequencies above 30 Hz, reaching 100 m/s or more at some frequencies. The wavelength of the Rayleigh wave at a frequency of 30 Hz is 4.5 m. When the distance from the source is three times this wavelength, the reflected Rayleigh waves become

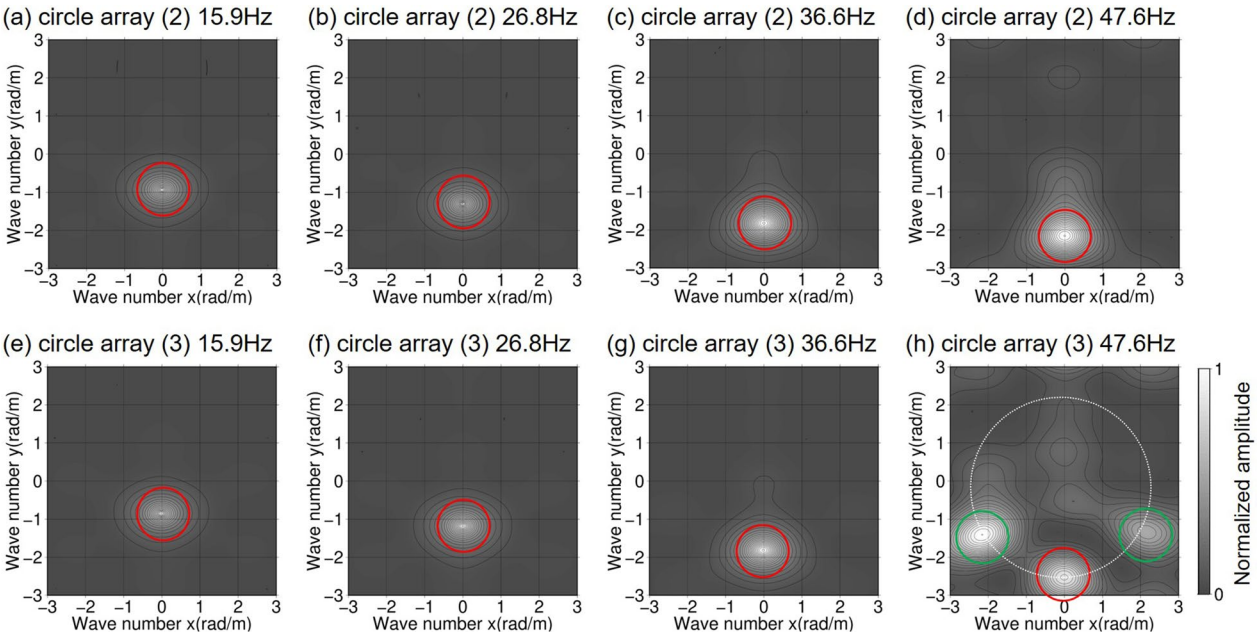

Fig. 6 F-K spectra from synthetic velocities recorded at frequencies of (**a**) 15.9, (**b**) 26.8, (**c**) 36.6 and (**d**) 47.6 Hz in array (2) and at frequencies of (**e**) 15.9, (**f**) 26.8, (**g**) 36.6 and (**h**) 47.6 Hz in array (3). Horizontal and vertical axes are wavenumbers in the perpendicular and longitudinal axes of the embankment. Gray shading represents the normalized power of the synthetic waveform at each wavenumber. The white dotted line in h) represents the wavenumber of the fundamental mode Rayleigh wave

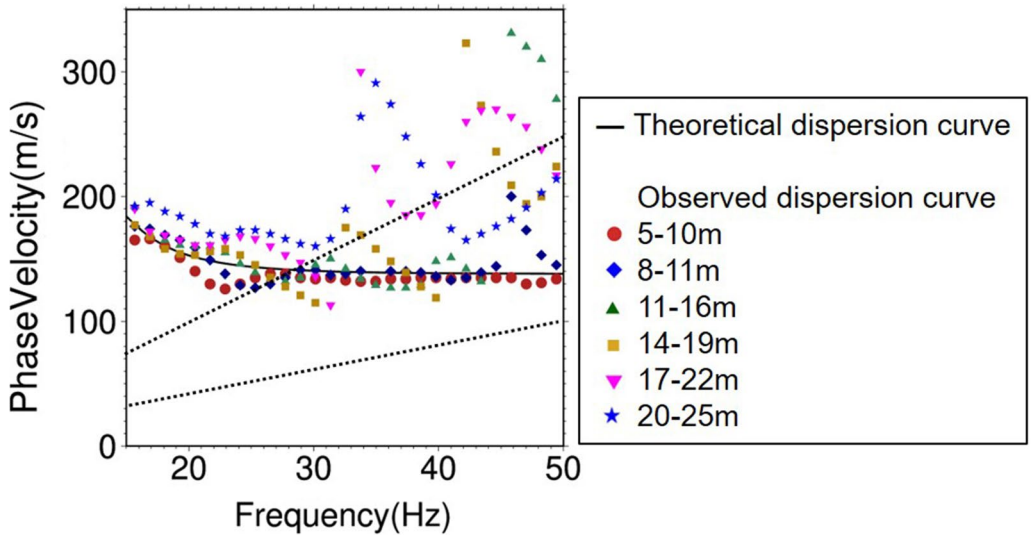

Fig. 7 Rayleigh wave phase velocity from synthetic vertical motions in Fig. 3 in 5 m ranges of distance from the source (5–10 m, 8–13 m, 11–16 m, 14–19 m, 17–22 m and 20–25 m). Plotted points represent observed phase velocity in each distance range and the solid line represents the theoretical Rayleigh wave phase velocity. The two dotted lines indicate the maximum and minimum wavelengths resolved by the linear array. The frequency bands of capable wavelength are focused

more dominant than the direct Rayleigh wave. It is, therefore, difficult to properly calculate the dispersion curves.

Result of numerical tests with model B

Synthetic waveforms

Figure 8a shows snapshots of the synthetic velocities on the surface of model B. Red arrows represent the arrivals

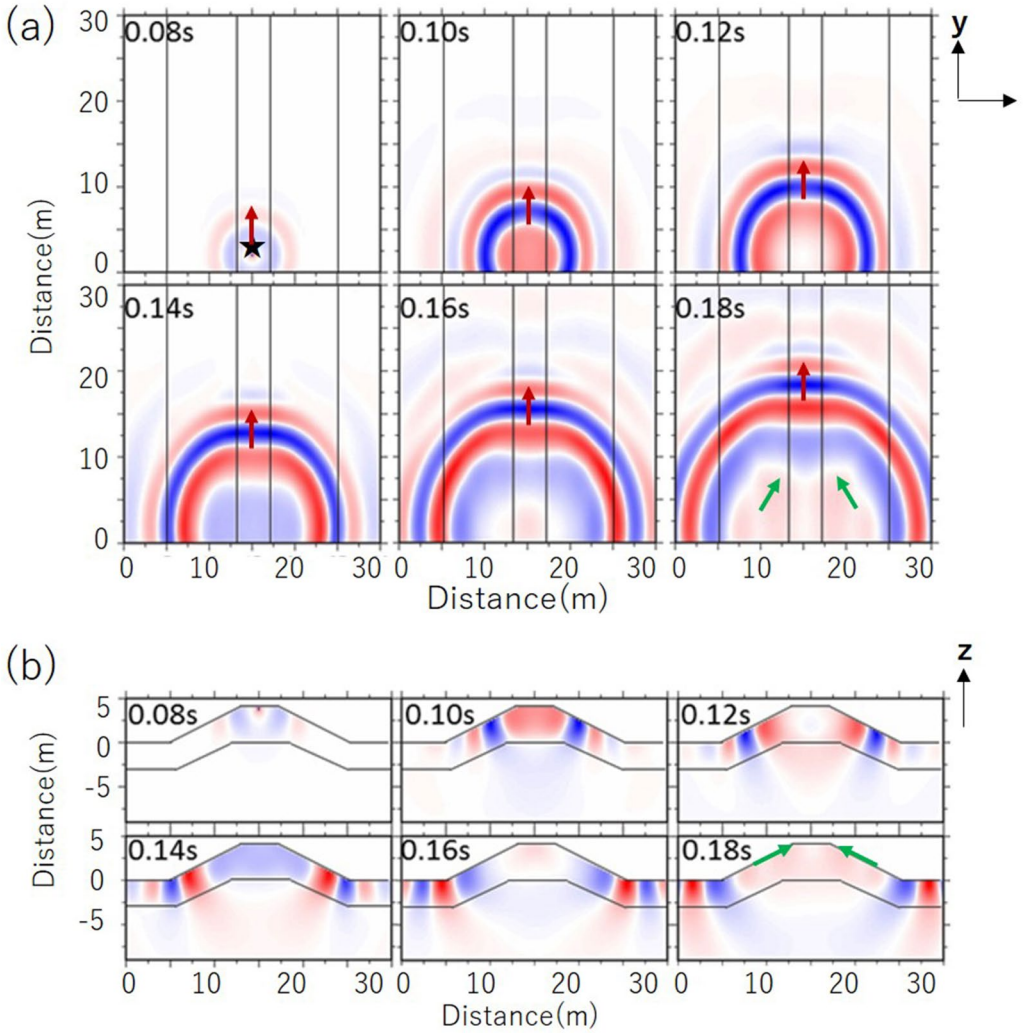

Fig. 8 Snapshots of synthetic vertical velocities (**a**) on surface and (**b**) in cross-section including the source point of model B. Colors represent the amplitude of waves propagating along the surface

of the direct Rayleigh wave. Green arrows represent those of the reflected Rayleigh waves. The amplitude of the reflected Rayleigh waves is considered to be smaller in model B than A. Figure 8b shows snapshots of the synthetic velocities of the embankment cross-section including the source. The reflected Rayleigh wave generated at the bottom edge of the embankment has a small amplitude and difficult to see. Figure 9 shows the vertical component of the synthetic velocities calculated at the points along the linear array in model B. A red arrow marks the initial rise point of the arrival of the direct Rayleigh wave propagating along the linear array from the source, while a green arrow represents the arrival of the reflected Rayleigh waves. The amplitudes of the reflected Rayleigh waves in this figure are smaller than those in model A (c.f. Figure 4). Models A and B have the same surface topography, but the positions of the edge of the velocity

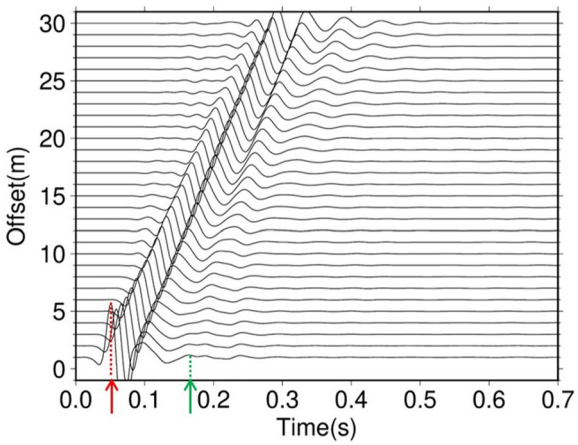

Fig. 9 Synthetic vertical velocities calculated along the linear array on the crest of model B. Red and green arrows indicate direct waves and reflected Rayleigh waves, respectively

boundaries are different. Therefore, it is clear that the generation of the reflected Rayleigh waves depends more on the position and shape of the velocity boundary than on the shape of the embankment surface.

Rayleigh waves dispersion curves

Figure 10 presents dispersion images of the synthetic velocities shown in Fig. 9 in a distance range of 20 or 10 m from the source along the linear array. The difference between the observed dispersion curves and the theoretical ones is small at any frequency. The influence of the reflected Rayleigh waves on the phase velocity is less than in model A.

Figure 11 shows the dispersion curves of the phase velocity obtained from the synthetic waves recorded in a range of 5 m along the survey line. The dispersion curves obtained at relatively small distances from the source (5–10 m and 8–13 m) fit well with the theoretical values at any frequencies. The phase velocity differences at distances of 11–25 m are about 20 m/s at frequencies above 40 Hz. The increase in the discrepancy between the observed and theoretical phase velocities with distances from the source is much less than model A.

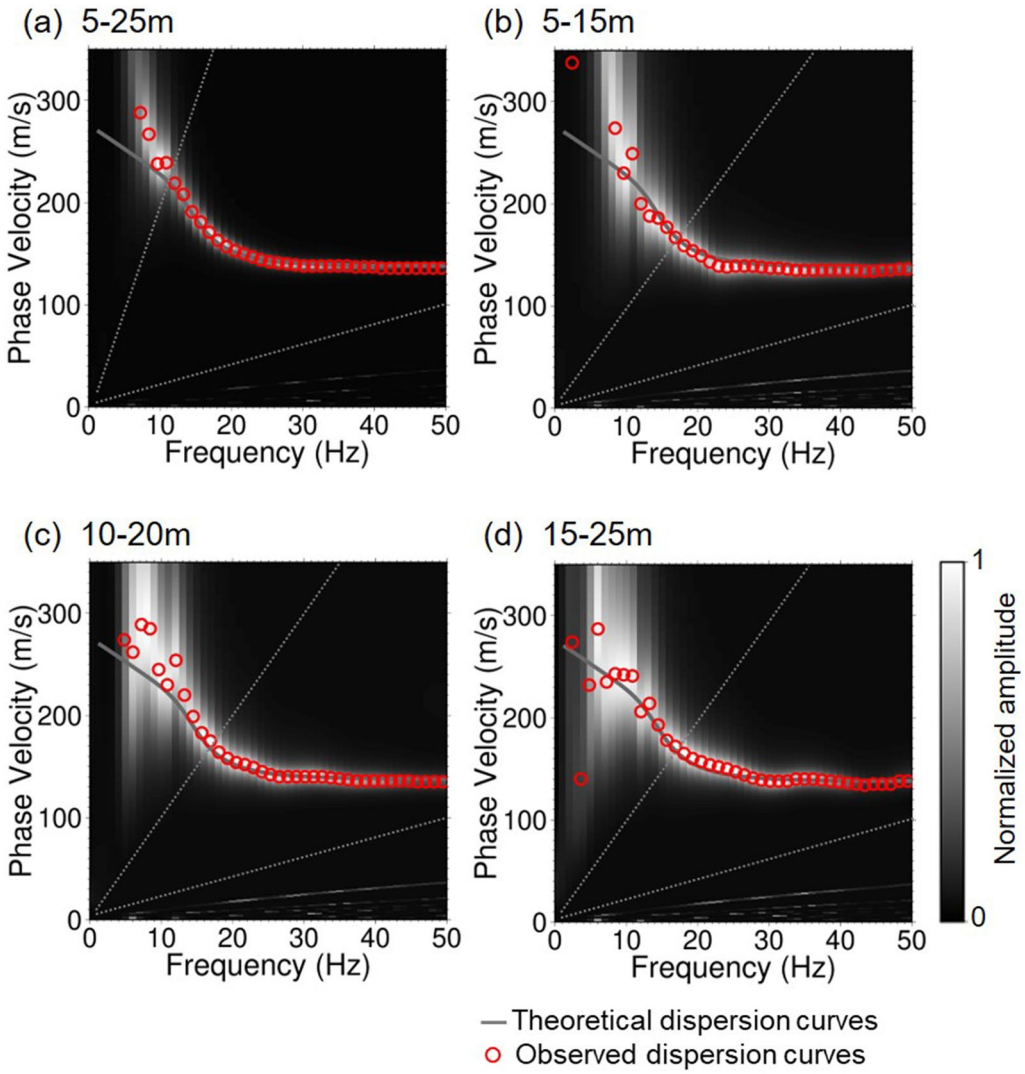

Fig. 10 Dispersion features of Rayleigh wave phase velocities obtained from synthetic vertical velocities in Fig. 9 for model B. Synthetic waveforms are analyzed in 20 or 10 m ranges from the source: **a** 5–25 m, **b** 5–15 m, **c** 10–20 m, **d** 15–25 m. Gray shading represents normalized power of synthetic velocity at each frequency. Open red dots represent observed phase velocities and the solid lines are the theoretical dispersion curves of the Rayleigh wave fundamental mode for the 1D profile beneath the linear array in the model. The two dotted lines indicate the maximum and minimum wavelengths resolved by the linear array. The frequency bands of capable wavelength are focused

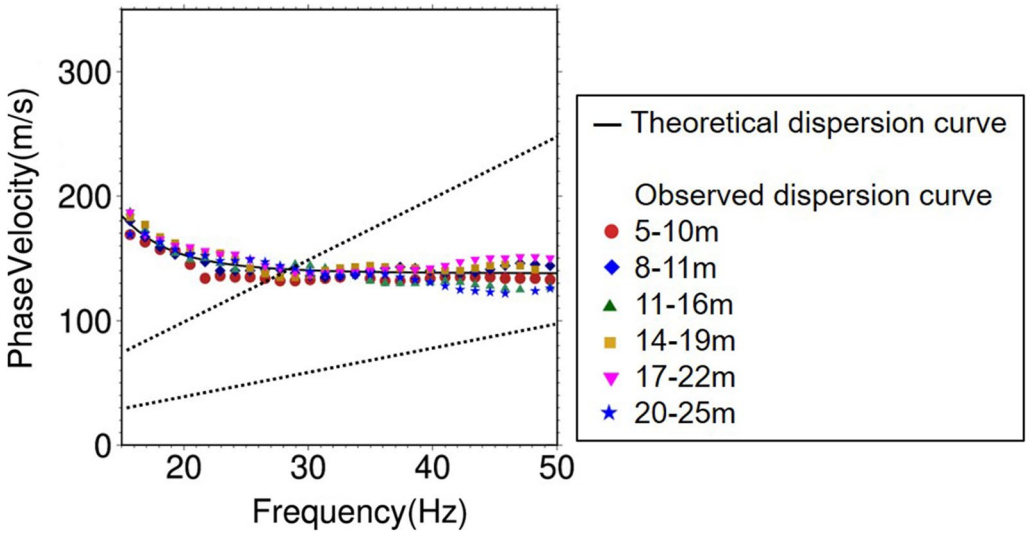

Fig. 11 Rayleigh wave phase velocity from synthetic vertical velocity in Fig. 9 for model B. Synthetic waveforms are analyzed in ranges of 5 m from the source: 5–10 m, 8–13 m, 11–16 m, 14–19 m, 17–22 m, 20–25 m. Plotted points represent observed phase velocities for the synthetic waves recorded at each source distance. The solid line represents the theoretical phase velocity of the fundamental mode Rayleigh waves. The two dotted lines indicate the maximum and minimum wavelengths resolved by the linear array, respectively. The frequency bands of capable wavelength are focused

Realistic embankment model

In this section, we discuss the effects of subsurface irregularities in the case of a realistic model of a river embankment. Figure 12a shows an S-wave velocity structure of a real river embankment obtained by an S-wave tomography (Suzuki and Kanazawa 2017). A model of embankment, shown in Fig. 12b, was developed from characterization with homogeneous layers in Fig. 12a. We refer to this as model C. The surface topography of this model is the same as models A and B, while the velocity boundary is set at different depths on the river (right) side and on the landward (left) side of the embankment. The physical parameters are the same as in the previous models.

Synthetic waveforms

Figure 13 shows snapshots of the surface velocities. Figure 14 shows the synthetic waveforms recorded in the linear array on the crest of model C. Travel times of the Rayleigh waves propagating along the left and right slopes of the embankment are different, with amplitudes on the left slope larger than those on the right slope. This is due to the difference in the position of the bottom edges of the velocity boundary. Since the velocity boundary at the bottom edge on the left side of the embankment is shallower and the layer is thinner than that on the right side, the Rayleigh wave generated at the bottom left edge of the embankment propagates on the slope in the direction of the crest with the large amplitude.

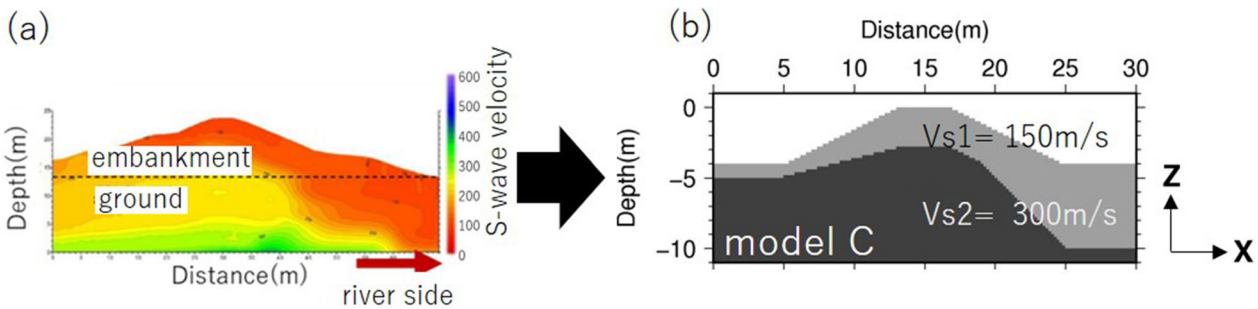

Fig. 12 Establishment of model C. **a** 2D S-wave velocity profile of river embankment. (Suzuki and Kanazawa 2017). **b** Cross-section of numerical model created with reference to real model. Height and crest width of the embankment are 2.75 m and 4 m and the 2D profile slope gradient is 1:2

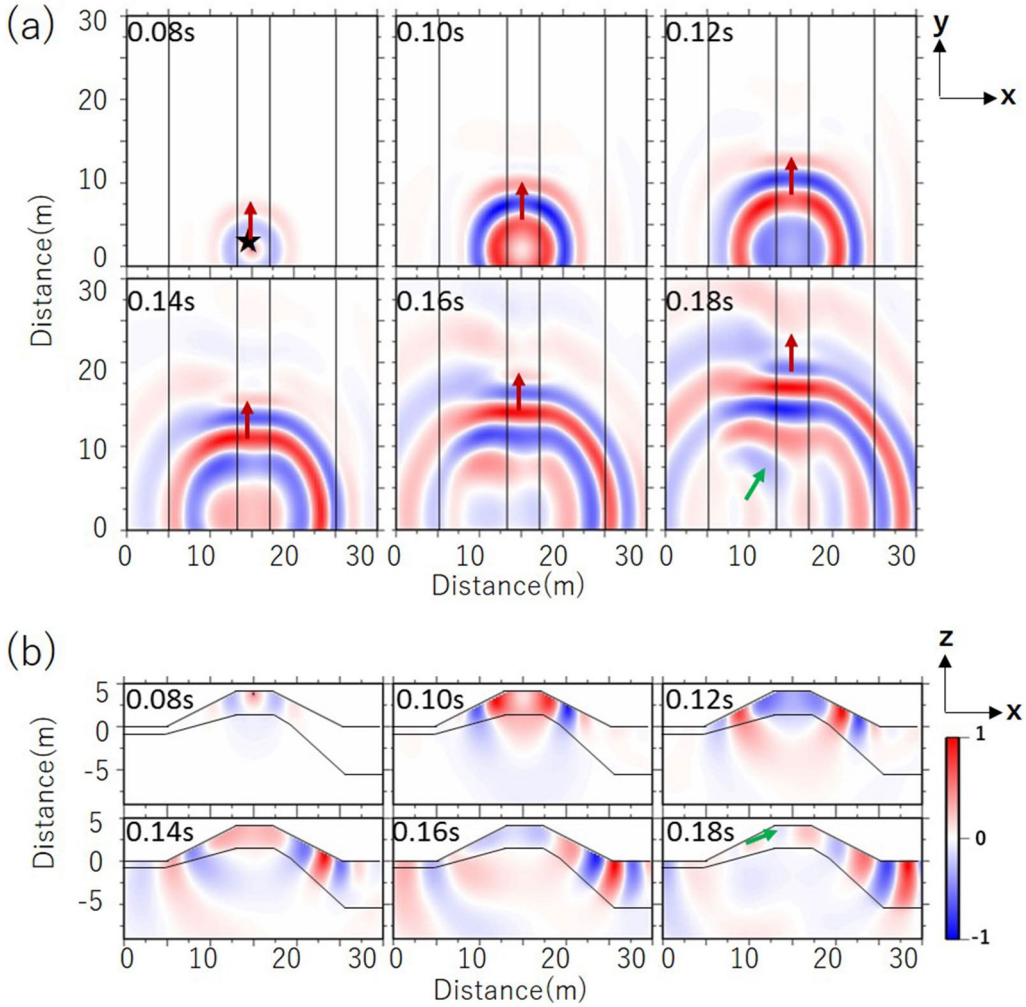

Fig. 13 Snapshots of synthetic vertical velocities (**a**) on surface and (**b**) in cross-section including the source point of model C. Colors represent the amplitude of the vertical component

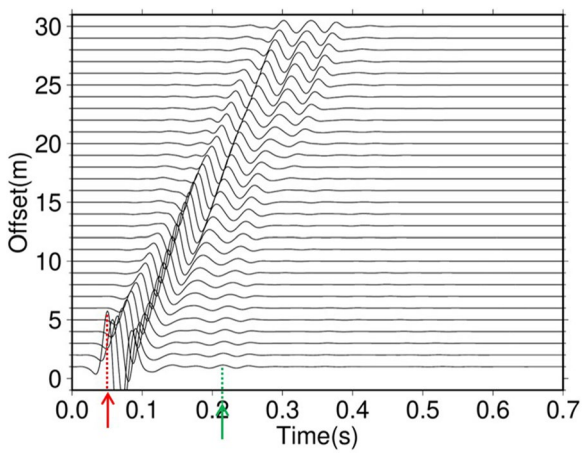

Fig. 14 Synthetic vertical velocities along linear array on the crest of model C. Red and green arrows indicate the direct wave and reflected Rayleigh waves, respectively

Rayleigh wave dispersion curves

Figure 15 shows the dispersion curves of the Rayleigh wave phase velocities for the synthetic waveforms in Fig. 14. When the distance range is 5–25 m (Fig. 15a), the discrepancy between the observed and theoretical phase velocities is about 40 m/s at frequencies below 20 Hz. The observed dispersion curves are similar to the theoretical ones when the distance range from the source is 5–15 m (Fig. 15b). This result is similar to those obtained in the experiments using models A and B. When the distance range is 10–20 m (Fig. 15c), a small discrepancy (< 30 m/s) between the observed and theoretical phase velocities is seen at frequencies of 20 Hz. The theoretical wavelengths of the fundamental mode Rayleigh wave are about 10 m at 20 Hz. A discrepancy was found when the phase velocity was obtained from the synthetic waveform at offset of more

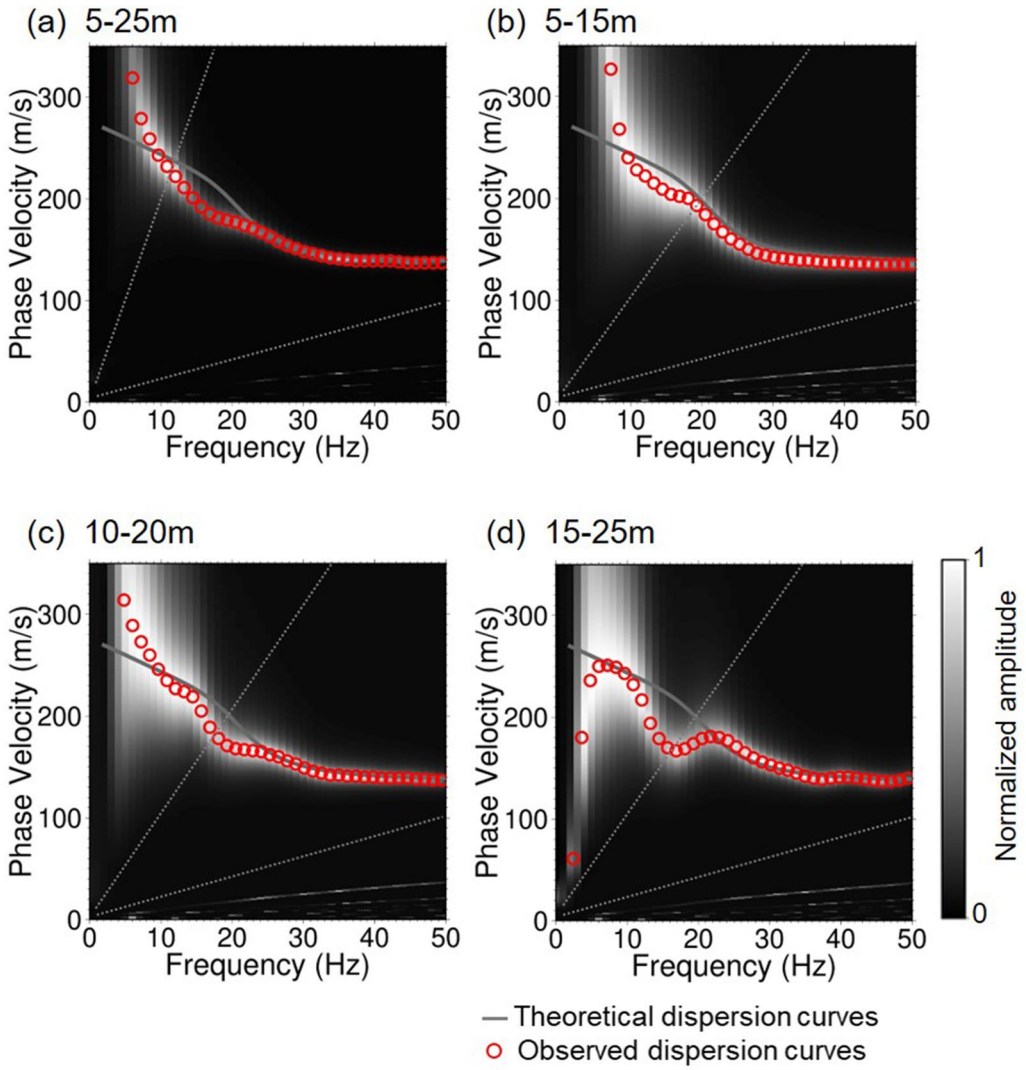

Fig. 15 Rayleigh waves phase velocities from synthetic vertical velocities in Fig. 14 for model C. Synthetic waveforms are analyzed in 20 or 10 m ranges from the source: **a** 5–25 m, **b** 5–15 m, **c** 10–20 m, **d** 15–25 m). Gray shading represents normalized power of synthetic waveform velocity at each frequency. Open red dots represent observed phase velocities and solid lines are the theoretical dispersion curves of the Rayleigh wave fundamental mode for the 1D profile beneath the linear array in the model. The two dotted lines indicate the maximum and minimum wavelengths resolved by the linear array, respectively. The frequency bands of capable wavelength are focused

than 15 m. Therefore, the reflected Rayleigh waves may be dominate over the direct Rayleigh wave when the source distance is more than 1.5 times the wavelength. In the distance range of 15–25 m (Fig. 15d), we can also see a small discrepancy of about 20 m/s at frequencies of 20 Hz. The discrepancy can be found in models A and C when the offset distance is long. However, the frequency at which the discrepancy between the observed and theoretical phase velocities for models A differs from that of model C. It is considered that the shape, depth and thickness of the edge part is so important for the frequency of the reflected Rayleigh waves.

Dispersion curve at high frequency

Figure 16 shows the dispersion curves obtained from the synthetic waves recorded in range of 5 m along the survey line. The observed phase velocities fit well with the theoretical ones at all frequencies and the ranges of array. The effects of the reflected Rayleigh waves are not significant at the high frequency in this model (Table 1).

Discussion

In models A and B, reflected Rayleigh waves were found in addition to the direct Rayleigh waves. The reflected Rayleigh waves have higher amplitude in model A than

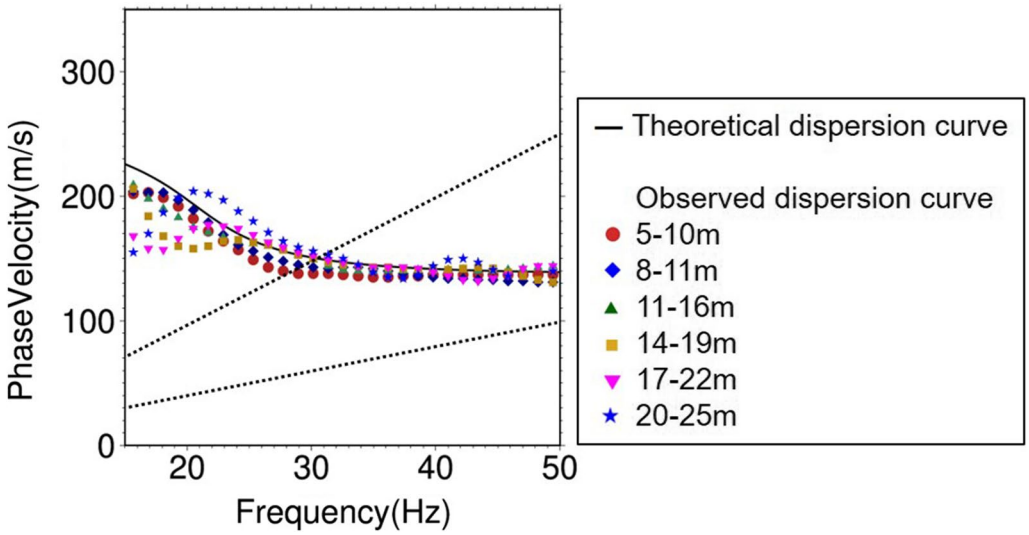

Fig. 16 Rayleigh waves phase velocity from synthetic vertical velocity in Fig. 14 for model C. Synthetic waveforms are analyzed in ranges of 5 m from the source: 5–10 m, 8–13 m, 11–16 m, 14–19 m, 17–22 m and 20–25 m. Plotted points represent the observed phase velocity recorded at each source distance. The solid line represents the theoretical dispersion curve of the fundamental mode Rayleigh wave for the model. The two dotted lines indicate the maximum and minimum wavelengths resolved by the linear array, respectively. The frequency bands of capable wavelength are focused

Table 1 Physical parameters of embankment models

Layer	S-wave velocity Vs (m/s)	P-wave velocity Vp (m/s)	Q-value *Q*	Density ρ (kg/m^3)
1	150	260	1000	1600
2	300	519	1000	1700

Table 2 The ratio of the observed and the theoretical phase velocity difference

Model	Source distance range [m]	Frequency [Hz]			
		10–20	20–30	30–40	40–50
A	5–20	3.2	2.5	3.6	34.0
	5–15	–	4.4	2.2	4.2
	10–20	–	5.1	4.3	90.8
	15–25	–	10.0	41.1	60.3
B	5–20	2.5	0.7	1.0	1.6
	5–15	–	2.9	2.6	2.3
	10–20	–	1.2	1.0	1.9
	15–25	–	2.6	0.8	1.8
C	5–20	10.8	3.3	2.1	1.7
	5–15	–	6.0	4.2	3.3
	10–20	–	4.5	1.6	1.3
	15–25	–	3.3	1.5	1.0

The unit is %

in model B. The main difference between the two models is the position of the velocity boundary; when the velocity boundary is located on the ground surface and the edge has a role to trap the waves inside the surface layers, the reflected surface waves generally have higher amplitude (e.g., Kawase and Sato 1992). In model A, the velocity boundary is at the ground surface at the bottom of the embankment. It can easily and effectively generate and trap the Rayleigh wave within the embankment. However, the velocity boundary in model B is in the subsurface and the amplitude of the reflected wave is small. The reflected Rayleigh wave from the left slope of the embankment is only dominant in model C, where the velocity boundary is close to the bottom of the embankment. These results indicate that reflected Rayleigh waves are likely to arise when the velocity boundary is located near the bottom edge of the embankment and the layer is narrow. The actual topographical shape of the embankment itself does not have a large effect on the generation of reflected waves.

Table 2 shows the differences value between observed and theoretical phase velocities for each model, source offset distance and frequency. The incorrect estimations of the direct Rayleigh wave phase velocity occurred in model A and C because of the contamination of the direct Rayleigh wave by the reflected Rayleigh waves. In both models, the difference between the observed phase velocity and the theoretical (estimated) one increases with distances from the source. This tendency was especially significant at high frequencies (30 Hz <) in model A and at low frequencies (< 30 Hz) in model C. Also, in model A, when the source offset distance is more than 15 m, a large difference was seen even at low frequency. In model B, we found little effect of the reflected Rayleigh wave on the phase velocity estimation. These demonstrate that the effects of reflected Rayleigh waves on observed phase velocity depend on the location and shape of the velocity boundary.

However, when the source offset distance was within 1.5 times the wavelength in model A, and 2.5 times in model C, the reflected Rayleigh wave does not contaminate the direct wave, and an appropriate phase velocity was obtained from the synthetic waveforms. The minimum source offset distance must be considered as well as the maximum one. Rayleigh waves are not well developed if the distance from the source is less than half of the wavelength (Stokoe et al. 1994). Therefore, it is necessary to use waveforms obtained where the source offset distance is at least 0.5 to 1.5 times of the wavelengths of Rayleigh waves to calculate the phase velocity.

Conclusions

Numerical experiments were conducted to investigate the assumptions of the horizontally layering in the application of the surface wave method to river embankments. The characteristics of the synthetic wave propagation and the Rayleigh wave phase velocity were investigated for several models with different subsurface irregularities. All models have exactly same surface topography. The results show that the Rayleigh wave propagating along the observation line on the embankment crest can be contaminated by the reflected Rayleigh waves generated at the bottom edges of the embankment. The contamination is pronounced when the velocity boundary is located on or near the bottom edges of the embankment, while the reflected Rayleigh waves are less dominant in models with deeper velocity boundaries. Therefore, the role of subsurface structural irregularities is more significant than that of surface topographical irregularities in the generation of the reflected Rayleigh waves in embankments.

We also found that biases in the phase velocity estimates of Rayleigh waves could depend on the source offset distance. In our numerical models, even if a large reflected Rayleigh wave was generated, it is effective to use the waveform record at a source offset distance of at most 1.5 times the wavelength of the Rayleigh wave to estimate the phase velocity. In addition, it is necessary to excluded waveforms obtained where the source offset distance is less than 0.5 times of the wavelengths of Rayleigh waves from the phase velocity calculation, because Rayleigh wave does not occur at that distance.

Appendix

In this study, we employ a 3D finite difference method (FDM) with 8th-order accuracy in space and second-order accuracy in time to solve the equation of motion. The grid spacing is set to 0.125 m in all three directions. Prior to starting the numerical experiments, the accuracy of the finite difference (FD) calculations was confirmed using several FD schemes. The candidates for the spatial finite difference schemes in this confirmation process were 4th-order, 8th-order (Furumura 2009) and 16th-order approximations. We refer the above existing FD equations and only explain the 16-order approximation in the following.

In the FDM, a 3D region is discretized with a fine grid spacing ($\Delta x, \Delta y, \Delta z$). The 16th-order spatial differentials based on the 3D staggered FDM are defined by

$$
\begin{aligned}
\frac{\partial}{\partial x}\sigma_{pq}(x,y,z) = \frac{1}{\Delta x}\Bigg[& \frac{3\times 131\times 1229\times 13241\times 611}{2^4\times 23\times 4211\times 204449549}\left\{\sigma_{pq}\left(x+\frac{\Delta x}{2},y,z\right)-\sigma_{pq}\left(x-\frac{\Delta x}{2},y,z\right)\right\} \\
& -\frac{41\times 8240019699787}{2^5\times 5\times 23\times 4211\times 204449549}\left\{\sigma_{pq}\left(x+\frac{3\Delta x}{2},y,z\right)-\sigma_{pq}\left(x-\frac{3\Delta x}{2},y,z\right)\right\} \\
& +\frac{151\times 277\times 40123\times 217411}{2^5\times 5^2\times 23\times 4211\times 204449549}\left\{\sigma_{pq}\left(x+\frac{5\Delta x}{2},y,z\right)-\sigma_{pq}\left(x-\frac{5\Delta x}{2},y,z\right)\right\} \\
& -\frac{61\times 79\times 14717\times 2386193}{2^6\times 5^3\times 23\times 4211\times 204449549}\left\{\sigma_{pq}\left(x+\frac{7\Delta x}{2},y,z\right)-\sigma_{pq}\left(x-\frac{7\Delta x}{2},y,z\right)\right\} \\
& +\frac{37\times 9222940953731}{2^7\times 5^3\times 23\times 4211\times 204449549}\left\{\sigma_{pq}\left(x+\frac{9\Delta x}{2},y,z\right)-\sigma_{pq}\left(x-\frac{9\Delta x}{2},y,z\right)\right\} \\
& -\frac{29\times 543349\times 6691163}{2^3\times 5^4\times 13\times 113\times 86269526129}\left\{\sigma_{pq}\left(x+\frac{11\Delta x}{2},y,z\right)-\sigma_{pq}\left(x-\frac{11\Delta x}{2},y,z\right)\right\} \\
& +\frac{3\times 89866480573339}{2^8\times 5^5\times 23\times 4211\times 204449549}\left\{\sigma_{pq}\left(x+\frac{13\Delta x}{2},y,z\right)-\sigma_{pq}\left(x-\frac{13\Delta x}{2},y,z\right)\right\} \\
& -\frac{29\times 696119\times 6687293}{2^9\times 5^6\times 23\times 4211\times 204449549}\left\{\sigma_{pq}\left(x+\frac{15\Delta x}{2},y,z\right)-\sigma_{pq}\left(x-\frac{15\Delta x}{2},y,z\right)\right\}\Bigg], \qquad (3)
\end{aligned}
$$

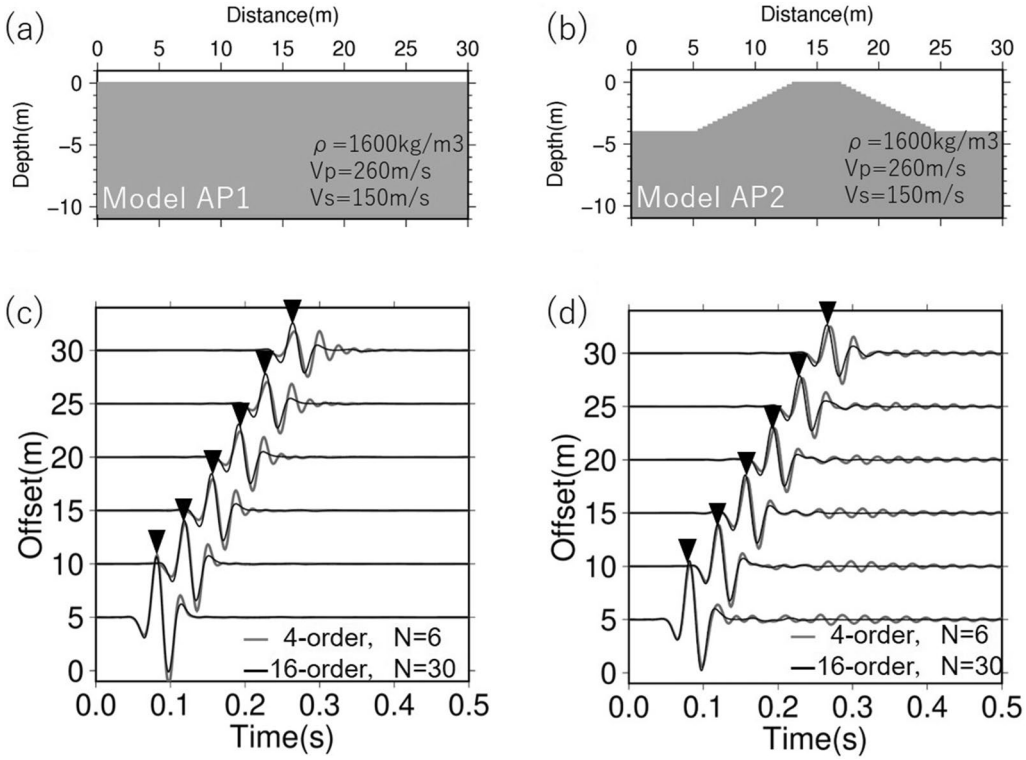

Fig. 17 **a** Cross-section of model AP1 with flat surface. **b** Cross-section of homogeneous embankment model called model AP2. ρ: density of the model. Vp: P-wave velocity of the model. Vs: S-wave velocity structure of the model. Q: *Q*-value of the model. **c** Synthetic vertical velocities recorded along linear array (1) in Fig. 2a for model AP1. **d** Synthetic vertical velocities recorded along linear array (1) in Fig. 2a for model AP2. N: Number of grid points per shortest wavelength

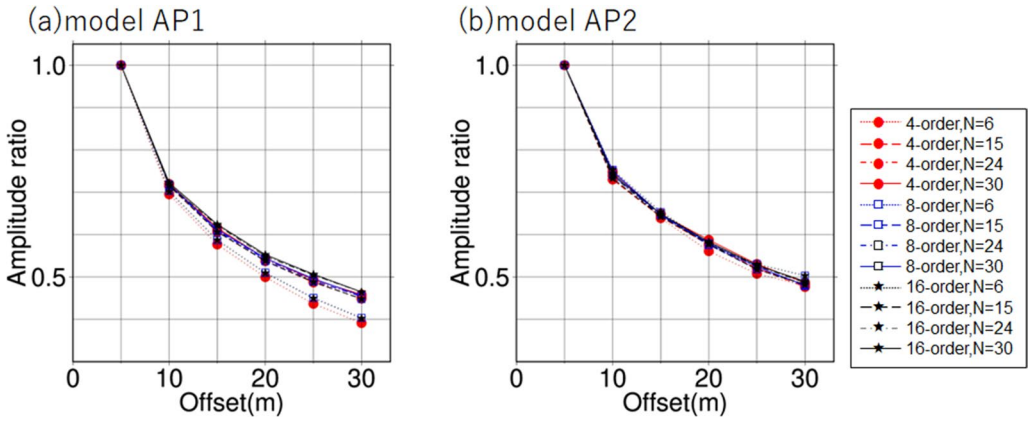

Fig. 18 Comparison of surface velocity amplitude ratios normalized by the synthetic waves calculated with the 16-order FD scheme and $N=30$. **a** Model AP1 and (**b**) model AP2. Plotted points represent FD approximations of the spatial differences and grid spacings. *N* is the number of grid points per shortest wavelength

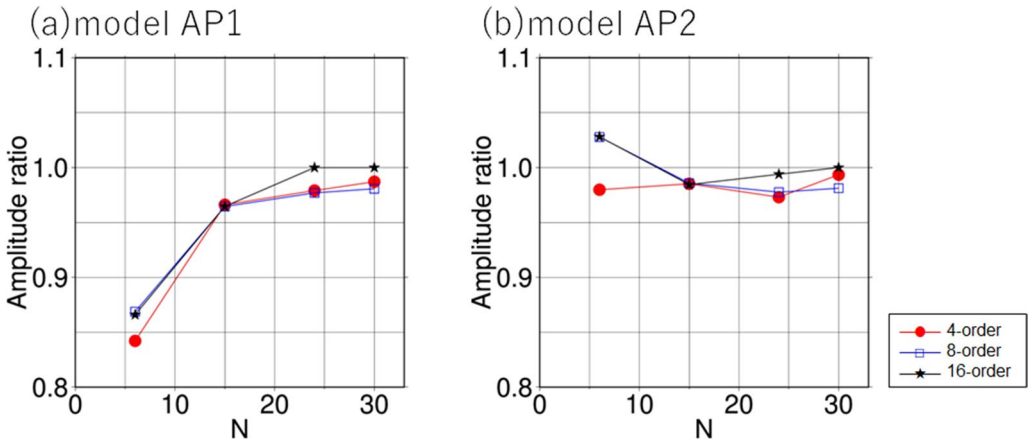

Fig. 19 Comparison of amplitude ratios of surface velocities at a distance of 30 m. **a** model AP1 and (**b**) model AP2. Amplitudes are normalized by the synthetic waves calculated with the 16-order FD scheme and $N=30$. Plotted points represent FD approximations of the spatial difference. N is the number of grid points per shortest wavelength

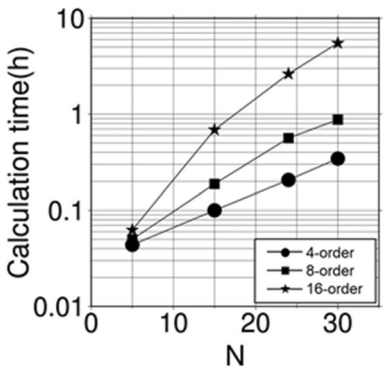

Fig. 20 Comparison of computation time required to obtain synthetic waveforms with a duration of 0.1 s. Plotted points represent spatial finite differences. N is the number of grid points per shortest wavelength

where $\sigma_{pq}(p, q = x, y, z)$ is the stress component.

The numerical test was performed with the calculated waves using the linear array (1) defined in Fig. 2a in models AP1 and AP2 (Appendix Fig. 17a, b). The model is divided into four areas for a parallel computation. We test 12 conditions in the FD calculations, with the three FD approximations and four grid spacings (which are set in terms of the number of grid points per shortest wavelength). The examined spatial finite differences are the 4-order, 8-order and 16-order approximations. The numbers of grid points per shortest wavelengths, *N*, were set to 6, 15, 24 and 30.

Appendix Fig. 17c, d show the vertical components of the synthetic velocities in models AP1 and AP2, respectively. The gray lines are the synthetic waveforms from

the 4-order spatial finite difference calculations and $N=6$. Black lines show the waveforms for the 16-order accuracy and $N=30$. The effects of the numerical dispersion can be seen after the direct wave only when N is 6, regardless of the accuracy. In Appendix Fig. 18, the amplitude of the synthetic direct waves at each distance from the source for each model is normalized by the maximum amplitude of all the traces. When N is 15 or more, the same decreasing trend of amplitudes is seen. When N is 6, the attenuation is slightly faster with the offsets in Appendix Fig. 18a. Similarly, the decrease of the amplitudes is similar when N is greater than 15 in Appendix Fig. 18b.

Appendix Fig. 19 compares, for models AP1 and AP2, the amplitudes of the synthetic direct wave at a distance of 30 m, normalized by the amplitude of the synthetic wave from the calculation using the FD with 16-order accuracy and N = 30. In Appendix Fig. 19a, the amplitude ratios converge when N is more 24 regardless of the spatial finite differences. In Appendix Fig. 19b, the amplitude ratios converge when N is greater than 15. This result demonstrates the influence of the grid size on the wave reflection from the slope of the embankment. Rayleigh waves propagating along the slope are influenced by the angle of the slope (Bohlen and et al. 2006). Under the conditions set in this model, the amplitudes of Rayleigh waves generated at the edge of the embankment and propagating to the observation line converges when N is 15 or more.

Appendix Fig. 20 compares the computation time required to generate synthetic waves with a duration of 0.1 s. The computation time rises significantly for the spatial finite difference calculations with the 16-order accuracy because the grid spacing is reduced, which increases the number of the grid points in the numerical model. Taking into account calculational stability as well as computation time, we chose to do all spatial finite difference calculations in the numerical experiments with the 8th-order accuracy and 24 grids per shortest wavelength among the examined cases.

Abbreviation

FDM Finite difference method

Acknowledgements

We thank Kosuke Chimoto at Kagawa University for the support provided in carrying out the numerical simulations in this study.

Author contributions

SM conducted the analysis. SM and HY drafted the manuscript. All authors read and approved the final manuscript.

Funding

Not applicable.

Availability of data and materials

The datasets used and/or analyzed during the current study are available from the corresponding author on reasonable request.

Declarations

Ethics approval and consent to participate

Not applicable.

Consent for publication

Not applicable.

Competing interests

The authors declare that they have no competing interests.

Author details

[1]Taisei Corporation (Former Tokyo Institute of Technology), 344-1, Nase-Cho, Totsuka-Ku, Yokohama, Kanagawa 245-0051, Japan. [2]Tokyo Institute of Technology, 4259 Nagatsuta, Midori-ku, Yokohama, Kanagawa 226-8503, Japan.

Received: 26 May 2022 Accepted: 19 August 2023
Published online: 08 September 2023

References

Capon J (1969) High-resolution frequency-wavenumber spectrum analysis. Proc IEEE 57:1408–1418. https://doi.org/10.1109/PROC.1969.7278

Cerjan C, Kosloff D, Kosloff R, Reshef M (1985) A nonreflecting boundary condition for discrete acoustic and elastic wave equations. Geophysics 50:705–708. https://doi.org/10.1190/1.1441945

Clayton R, Engquist B (1977) Absorbing boundary conditions for acoustic and elastic wave equations. Bull Seismol Soc Am 67:1529–1540. https://doi.org/10.1785/BSSA0670061529

Foti S, Hollender F, Garofalo F, Albarello D, Asten M, Bard PY, Comina C, Cornou C, Cox B, Giulio GD, ForbrigerT HK, Lunedei E, Martin A, Mercerat D, Ohrnberger M, Poggi V, Renalier F, Sicilia D, Socco V (2017) Guidelines for the good practice of surface wave analysis: a product of the InterPACIFIC project. Bull Earthq Eng 16:2367–2420. https://doi.org/10.1007/s10518-017-0206-7

Furumura T (2009) Large-scale simulation of seismic wave propagation in 3D heterogeneous structure using the finite-difference method. Jishin 61:S83–S92. https://doi.org/10.4294/zisin.61.83. (**in Japanese with English abstract**)

Graves RW (1996) Simulating seismic wave propagation in 3D elastic media using staggered-grid finite differences. Bull Seismol Soc Am 86(4):1091–1106. https://doi.org/10.1785/BSSA0860041091

Hayashi K, Inazaki T (2007) Application of integrated geophysical technique to vulnerability assessment of levee (part 5): evaluation of surface-wave velocity measurements during levee excavation. In: Proceedings of the 117th SEGJ symposium, Japan, 6–8 October 2007 (**in Japanese**)

Hayashi K, Suzuki H (2004) CMP cross-correlation analysis of multi-channel surface-wave data. Explor Geophys 35(1):7–13. https://doi.org/10.1071/EG04007

Kawase H, Sato T (1992) Simulation analysis of strong motions in the Ashigara Valley considering one- and two-dimensional geological structures. J Phys Earth 40:27–56. https://doi.org/10.4294/jpe1952.40.27

Kim JT, Kim DS, Park HJ, Bang ES, Kim SW (2010) Evaluation of the applicability of the surface wave method to rock fill dams. Explor Geophys 41:9–23. https://doi.org/10.1071/EG09054

Luo Y, Xia J, Liu J, Xu Y, Liu Q (2009) Research on the middle-of-receiver-spread assumption of the MASW method. Soil Dyn Earthq Eng 29:71–79. https://doi.org/10.1016/j.soildyn.2008.01.009

McMechan GA, Yedlin MJ (1981) Analysis of dispersive waves by wave field transformation. Geophysics 46(6):869–874. https://doi.org/10.1190/1.1441225

Miller RD, Xia J, Park CB, Ivanov JM (1999) Multichannel analysis of surface waves to map bedrock. Leading Edge 18(12):1392–1396. https://doi.org/10.1190/1.1438226
Mittet R (2002) Free-surface boundary conditions for elastic staggered-grid modeling schemes. Geophysics 67(5):1616–1623. https://doi.org/10.1190/1.1512752
Nazarian S, Stokoe KH II, Hudson WR (1983) Use of spectral analysis of surface waves method for determination of moduli and thicknesses of pavement systems. Transpt Res Record 930:38–45
Okada H (2003) The microtremor survey method. Geophysical Monograph Series Vol 12 Society of Exploration Geophysicists, Tulsa, Oklahoma.
Park CB, Miller RD, Xia J (1998) Imaging dispersion curves of surface waves on multi-channel record. SEG Tech Progr Expand Abstracts 1998:1377–1380
Park CB, Miller RD, Xia J (1999) Multichannel analysis of surface waves. Geophysics 64(3):800–808. https://doi.org/10.1190/1.1444590
Richart FE, Hall JR, Woods RD (1970) Vibrations of soils and foundations. Prentice-Hall Inc, USA
Socco LV, Foti S, Boiero D (2010) Surface-wave analysis for building near-surface velocity models-established approaches and new perspectives. Geophysics 75(5):7583–75102. https://doi.org/10.1190/1.3479491
Stokoe KH, Wright GW, James AB, Jose MR (1994) Characterization of geotechnical sites by SASW method. In: Geophysical characterization of sites. Oxford Publ, Oxford
Suzuki H., Kanazawa J (2017) Inspection of integrated geophysical exploration results by rock physics technique, In: Proceedings of the 137th SEGJ symposium, Japan, 8–10 November 2017 (**in Japanese with English abstract**)
Xia J, Miller RD, Park CB (1999) Estimation of near-surface shear-wave velocity by inversion of Rayleigh waves. Geophysics 64(3):691–700. https://doi.org/10.1190/1.1444578
Xia J, Chen C, Li PH, Lewis MJ (2004) Delineation of a collapse feature in a noisy environment using a multichannel surface wave technique. Geotechnique 54(1):17–27. https://doi.org/10.1680/geot.2004.54.1.17
Xia J, Xu Y, Miller RD (2007) Generating an image of dispersive energy by frequency decomposition and slant stacking. Pure Appl Geophys 164:941–956. https://doi.org/10.1007/s00024-007-0204-9
Yilmaz O (1987) Seismic data processing. Society of Exploration Geophysicists, Tulsa, Oklahoma
Zeng C, Xia J, Miller RD, Tsoflias GP (2012) An improved vacuum formulation for 2D finite-difference modeling of Rayleigh waves including surface topography and internal discontinuities. Geophysics 77(1):T1–T9. https://doi.org/10.1190/geo2011-0067.1

Publisher's Note